Phase stability of stress-sensitive Ag$_2$CO$_3$ silver carbonate at high pressures and temperatures

D. Santamaría-Pérez [a,*], L. Pavic [a], R. Chuliá-Jordán [a,b], J. Ruiz-Fuertes [c], C. Popescu [d], A. Otero-de-la-Roza [e]

[a] *Departamento de Física Aplicada-ICMUV, Universitat de València, MALTA Consolider Team, 46100, Valencia, Spain*
[b] *Departamento de Didáctica de las Ciencias Experimentales y Sociales, Universitat de Valencia, 46022, Valencia, Spain*
[c] *DCITIMAC, Universidad de Cantabria, MALTA Consolider Team, 39005, Santander, Spain*
[d] *CELLS-ALBA Synchrotron Light Facility, Cerdanyola del Vallés, 08290, Barcelona, Spain*
[e] *Departamento de Química Física y Analítica, Facultad de Química, Universidad de Oviedo, MALTA Consolider Team, 33006, Oviedo, Spain*

ABSTRACT

Silver carbonate (Ag$_2$CO$_3$) is a material currently used for artificial carbon storage. In this work, we report synchrotron X-ray powder diffraction (XRD) experiments under high pressure and high temperature in combination with density-functional theory (DFT) calculations on silver carbonate up to 13.3 GPa. Two pressure-induced phase transitions were observed at room temperature: at 2.9 GPa to a high-pressure (HP1) phase and at 10.5 GPa to a second high-pressure phase (HP2). The facts that a) the HP2 phase can be indexed with the initial $P2_1/m$ structure, b) our DFT calculations predict the initial structure is stable in the entire pressure range, and c) the HP2 phase is stable under decompression suggest that the intermediate HP1 phase is a product of the appearance of non-hydrostatic stresses in the sample. The observed structural transformations are associated to a high sensitivity of this compound to non-hydrostatic conditions. The compressibility of Ag$_2$CO$_3$ has also been determined, showing the c axis is the most compressible and that the bulk modulus increases quickly with applied pressure. We attribute both observations to the weak nature of the closed-shell Ag–Ag interactions in this material. The behavior of Ag$_2$CO$_3$ under heating at approximately 3 GPa was also studied. No temperature-induced phase transitions were found at this pressure, and the thermal expansion was determined to be relatively high for a carbonate.

1. Introduction

World countries expressed concern about the problems of increasing environmental pollution and stressed the need of action [1]. One of the main environmental threats is the high concentration of anthropogenic "greenhouse" gases, especially CO$_2$, in the Earth's atmosphere, derived mainly from the combustion of fossil fuels. This is the main cause of global warming and the acidification of the oceans. To mitigate climate change, it is urgent to develop strategies for the development of stable carbon dioxide capture/recovery technologies.

Natural processes occurring in the interior of the Earth suggest that carbon can be permanently sequestered by mineral carbonation [2–5]. Therefore, the understanding of the chemical reactivity of carbon dioxide and the determination of the stability of formed carbonate phases could therefore be part of the comprehensive set of solutions to address

the aforementioned environmental problem [6–8]. This approach offers three main advantages: (i) Carbonation reactions are thermodynamically favorable. (ii) Raw materials are abundant. (iii) The storage of CO$_2$ by carbonation can be considered permanent since carbonates tend to be chemically stable, thus minimizing environmental risks [9,10]. The methodology of several CO$_2$ removal systems is based on chemisorption, including the silver oxide (Ag$_2$O) carbonation system designed for life support applications in spacecrafts. Silver oxide reacts with carbon dioxide in the presence of water to yield silver carbonate and the chemisorption reaction can be reversed at elevated temperature [11]. For instance, a thermally regenerable CO$_2$ removal system is currently in the final stages of development for use in the portable life support subsystem housed in the extravehicular mobility unit worn by astronauts [12].

The carbonation product after the CO$_2$ chemisorption reaction on Ag$_2$O is silver carbonate Ag$_2$CO$_3$. The structure at ambient conditions of

this compound was firstly reported by Masse et al. from single-crystal X-ray diffraction (XRD) data [13]. The structure was found to be monoclinic, space group (S.G.) $P2_1/m$, and it was described either as built from (i) chains -Ag-[CO$_3$]-Ag-Ag-[CO$_3$]-Ag- along the b axis or (ii) stacks entirely composed of silver cations and carbonate anions perpendicular to the b axis [13,14]. Two high-temperature phases of Ag$_2$CO$_3$ were found at 423 K and 475 K, which were denoted as β (S.G. $P31c$) and α (S. G. P-62m) phases, respectively [14]. The first-order transitions to the high-temperature modifications roughly preserve the stacking of silver cations and carbonate units, but an atomic rearrangement happens whereby two [CO$_3$] groups are present in the asymmetric unit, instead of only one, as in the room-temperature phase. The decomposition to silver oxide and CO$_2$ occurs at 510 K at room pressure or at slightly higher temperatures when heating experiments are performed in a flow of carbon dioxide (increase of partial pressure) [15,16].

As far as we know, no study of the role of hydrostatic pressure and its combination with elevated temperatures has been undertaken. In order to give further insights into the crystal chemistry of AgCO$_3$ silver carbonate, we report in this work a joint high-pressure (HP) high-temperature (HT) experimental and computational investigation of its structural properties. We have characterized our sample by synchrotron powder X-ray diffraction under compression at room temperature and found two phase transitions at 2.9 and 10.5 GPa, respectively. The initial phase and the second high-pressure (densest) phase have the same structure, while the intermediate pressure-induced phase was tentatively indexed. The compressibility and anisotropy of all the phases were determined. HP-HT experiments allow obtaining the thermal expansion of the initial phase at a pressure of ~3 GPa and no high-temperature modifications were observed up to 512 K. Density Functional Theory (DFT) calculations on the AgCO$_3$ shed light into its phase stability and complement the experimental results.

2. Experimental details

A commercial polycrystalline yellow sample of silver carbonate (Sigma-Aldrich, 99.9%) was crushed with mortar and pestle to uniform the grain size. XRD measurements at ambient conditions using a Bruker D8 Advance diffractometer (Cu K$_\alpha$ radiation) confirmed that the ground sample had the structure previously reported (briefly described later) [13].

High-pressure angle-dispersive XRD experiments were conducted at the MSPD beamline of the ALBA-CELLS Synchrotron Light Source [17] with an incident monochromatic wavelength of 0.4246 Å focused to 20 × 20 μm^2 (full width at half maximum). The first run was carried out increasing pressure in small steps up to 13.3 GPa at room temperature. These measurements were performed in a membrane-type diamond-anvil cell (DAC) with diamond culets of 400 μm. Ag$_2$CO$_3$ powder was loaded in a 160 μm diameter hole of an Inconel gasket preindented to a thickness of 50 μm. Silicone oil was used as pressure-transmitting medium, which assures quasi-hydrosticity up to approximately 12 GPa [18,19]. Pressure was measured based on the Cu equation of state (EOS) [20]. A second run was performed by pressurizing the sample to 1.8 GPa and progressively increasing the temperature afterwards up to 3.1 GPa and 512 K. These measurements were performed in a membrane-type DAC with diamond culets of 300 μm. The pressure chamber has dimensions of 100 μm diameter and 40 μm thickness. The DAC was heated using a BETSA heating ring wrapped around the cell [21,22]. The temperature was measured using a K-type thermocouple attached to one of the diamond anvils, close to the gasket. The accuracy of the thermocouple on the temperature range covered by the experiments is ~0.4% [23]. In this second run, Cu powder and silicone oil were also included in the sample chamber to act as pressure marker [24] and pressure transmitting medium, respectively.

Detector calibration, correction of distortion, and integration to conventional 2θ-intensity XRD data were carried out with the Dioptas software [25]. The indexing and refinement of the powder patterns were

performed using the Unitcell [26], Powdercell [27] and Fullprof [28] program packages.

3. Computational details

Calculations were performed using density-functional theory with the projector augmented wave (PAW) method [29]. The Quantum ESPRESSO suite [30] (version 6.5) was used. Two functionals were employed, B86bPBE [31,32] and PBE [31], both incorporating dispersion interactions via the exchange-hole dipole moment (XDM) model [33–35]. The results from both functionals are very similar, so we report only the B86bPBE-XDM results. PAW datasets from the pslibrary [36] were used with valence electron numbers: 10 (Ag), 6 (O), and 4 (C). Plane-wave and electron density cutoffs of 100 and 1000 Ry, respectively, were used. The k-point grids were chosen for each phase examined to ensure a convergence of about 0.1 mRy in the total energy and 0.01 GPa in the pressure. The k-point grids for all phases studied were: 4 × 2 × 7 ($P2_1/m$ Ag$_2$CO$_3$) [13, this work], 2 × 2 × 2 ($P3_1/c$ Ag$_2$CO$_3$-HT-I) [14], 3 × 3 × 6 (P-62m Ag$_2$CO$_3$-HT-II) [14], 4 × 4 × 3 ($C2/c$ K$_2$CO$_3$–I-like) [37], 4 × 2 × 3 ($P2_1/c$ K$_2$CO$_3$-II-like) [38], 4 × 4 × 3 ($C2/m$ Na$_2$CO$_3$-like) [39], and 4 × 3 × 2 ($Pnma$ Rb$_2$CO$_3$-like) [40].

We first carried out constant-pressure structural optimizations on all structures at 0 and 50 GPa. Using the equilibrium geometries at these pressures, a uniform grid of 41 vol was set up, and constant-volume optimizations were performed in order to calculate the corresponding equations of state. The convergence thresholds for the geometry relaxations were 10^{-5} Ry in the energies and 10^{-4} Ry/Bohr in the forces. The calculated data was fitted with analytical polynomial strain average equations of state using gibbs2 [41,42] and, from these equations of state, the relative stability and thermodynamic properties were obtained.

4. Results and discussion

The atomic arrangement of Ag$_2$CO$_3$ silver carbonate at ambient conditions contrasts with that of other monovalent metal carbonates. Whereas in alkali metal carbonates (M_2CO$_3$, M = Na, K, Rb and Cs) the [CO$_3$] carbonate groups and the metal atoms alternate forming chains (the increasing size of the cation imparts a significant deviation from linearity), in Ag$_2$CO$_3$ stacks entirely composed of silver cations are found. This rather distinctive structure, previously reported from single-crystal XRD data [13], was confirmed by our XRD measurements and DFT calculations.

The Rietveld refinement of the ambient conditions XRD pattern shown in Fig. 1 was performed using, as initial model, the monoclinic $P2_1/m$ (space group No. 11) structure of Ag$_2$CO$_3$ reported in literature [13]. This yielded the lattice parameters, unit-cell volume, and the atomic coordinates shown in Table 1. These values are in agreement with those previously reported [13] and compare well with our DFT calculation results (also in Table 1), which overestimate the β angle by 3° and the unitcell volume by 4%.

The initial Ag$_2$CO$_3$ structure consists of chains of Ag atoms and [CO$_3$] carbonate units along the b axis in a sequence -Ag-[CO$_3$]-Ag-Ag-[CO$_3$]-Ag-, as it can be seen in Fig. 2a. Experimental (calculated) data show that the carbonate groups deviate 23° (25°) from being perpendicular to the c axis. The Ag atoms, on the other hand, form interconnected corrugated hexagonal layers normal to the b axis with Ag–Ag distances ranging from 2.87 to 3.61 Å (2.79–3.7 Å). Note that comparable flat hexagonal layers exist in face-centered cubic (fcc) elemental metallic silver, with distances of 2.88 Å. Therefore, some distances remain as in the elemental parent metal but others increase due to the presence of [CO$_3$] carbonate groups within this metallic Ag subarray. The existence of fragments of the parent metal structure suggests that this carbonate could be regarded as a "stuffed" silver compound, as proposed elsewhere for oxides [43–45]. In this particular metallic arrangement, the coordination of Ag by O atoms is quite irregular with two Ag–O distances of 2.24 Å (2.23 Å)
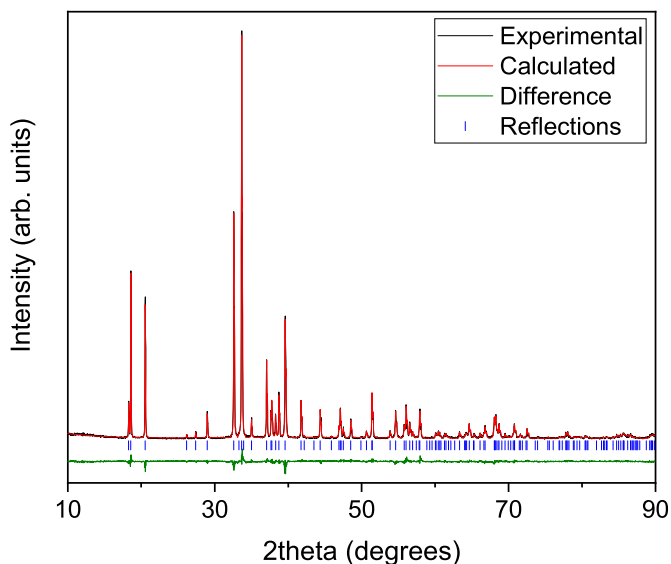
Fig. 1. Rietveld refinement of the XRD pattern of the Ag$_2$CO$_3$ sample at room conditions (λ_{Cu} = 1.5406 Å). The observed pattern is represented as a black line, the calculated profile for Ag$_2$CO$_3$ is represented as a red line, and the difference is depicted as a green line. Blue vertical marks indicate the position of Bragg reflections. (For interpretation of the references to colour in this figure legend, the reader is referred to the Web version of this article.)

Table 1

Lattice parameters, unit-cell volume and atomic coordinates of the monoclinic $P2_1/m$ Ag$_2$CO$_3$ silver carbonate at ambient pressure from powder (this work) and single-crystal [13] XRD diffraction and DFT calculations (this work). The unit-cell contains two formula units.

Parameters	Exp. This work	Exp. Literature [13]	Theor. This work
a (Å)	4.8506 (9)	4.852 (4)	4.9833
b (Å)	9.545 (2)	9.553 (8)	9.7468
c (Å)	3.2544 (4)	3.255 (4)	3.2421
β (°)	91.968 (2)	91.96 (1)	95.052
V (Å^3)	150.58 (8)	150.8 (4)	156.86
x_{Ag}	0.2115 (4)	0.2109 (2)	0.20187
y_{Ag}	0.0781 (2)	0.0781 (1)	0.07088
z_{Ag}	0.2188 (3)	0.2191 (2)	0.23843
x_C	0.265 (4)	0.270 (3)	0.28313
y_C	0.75	0.75	0.75
z_C	0.262 (3)	0.261 (4)	0.19539
x_{O1}	0.977 (2)	0.982 (2)	0.96050
y_{O1}	0.25	0.25	0.25
z_{O1}	0.887 (4)	0.889 (3)	0.98972
x_{O2}	0.390 (2)	0.390 (1)	0.40413
y_{O2}	0.637 (2)	0.6342 (7)	0.63529
z_{O2}	0.328 (3)	0.334 (2)	0.28649

forming 158° quasi-linear O–Ag–O linkages (161°), and three additional Ag–O contacts at 2.44 Å (x1), 2.72 Å (x1) and 2.98 Å (x1). Linear coordination is characteristic of silver oxides and it has been explained by the strong 3d-4s hybridization of the noble metal orbitals [46]. The characteristics of this Ag–O bonding can be finely tuned by the controlled application of external pressure which force electronic redistribution within the solid.

The Ag$_2$CO$_3$ compound was compressed at room temperature up to 13.3 GPa. Synchrotron powder XRD patterns at selected pressures are collected in Fig. 3. The XRD patterns could be indexed with the initial monoclinic $P2_1/m$ structure up to 2.5 GPa. Unfortunately, high-pressure XRD data present intensities that do not correspond to perfect randomly oriented powder, so only peak positions and not relative intensities could be used to the structural analysis. From the diffraction patterns collected at different pressures and our DFT calculations we extracted the evolution of the lattice parametersof this initial phase with

increasing pressure (see Table 2). The obtained evolution for the unit-cell parameters and the cell volume are plotted in Fig. 4a and b, respectively. The linear axial compressibilities, defined as $\kappa = -1/x(\partial x/\partial P)$ (where $x = a, b, c$), estimated from our experimental (calculated) data in the 0–2.5 GPa pressure range are $\kappa_{a0} = 3.98\ (15)\cdot10^{-3}$ GPa^{-1} (4.88 (14)$\cdot10^{-3}$ GPa^{-1}), $\kappa_{b0} = 3.10\ (9)\cdot10^{-3}$ GPa^{-1} (2.63 (3)$\cdot10^{-3}$ GPa^{-1}) and $\kappa_{c0} = 14.7\ (5)\cdot10^{-3}$ GPa^{-1} (13.1 (4)$\cdot10^{-3}$ GPa^{-1}), which evidence the strong anisotropy in this compound. The β angle continuously decreases with pressure at a rate of 1.06 (4)°/GPa (0.82 (2)°/GPa) in this range. Fig. 4a clearly shows that the most compressible axis is the *c*-axis. This response to external pressure arises from the fact that the relatively incompressible [CO$_3$] carbonate units lie approximately perpendicular to the *c* axis. The compressibility of this compound is directly attributable to the compression of Ag–Ag bonds (see Fig. 2). A third-order Birch-Murnaghan EOS [47] was fitted to our 0–2.5 GPa pressure-volume dataset (see Fig. 4) fixing the zero-pressure unit-cell volume to its measured value (V$_0$ = 150.58 Å^3), and yielding a bulk modulus (B$_0$), and its first-pressure derivative (B$'_0$) of B$_0$ = 37 (2) GPa, and B$'_0$ = 10 (3). These values are in good agreement with those obtained from our calculations, V$_0$ = 156.88 (3) Å^3, B$_0$ = 42.9 (2) GPa, and B$'_0$ = 7.22 (4). The high B$'_0$ value indicates that the bulk modulus B$_0$ increases considerably with increasing pressure, at a larger rate than any other reported carbonate [48–52].

Taking into account the good agreement found between experimental and theoretical data in lattice parameters, atomic arrangement and unit-cell compressibility data, we used data from our DFT calculations to study the variation of bond distances and polyhedral geometries with pressure. The large compressibility of the *c* axis results in the rapid decrease of the Ag–Ag distances parallel to the [0 0 1] direction under pressure, forming interconnected double chains of silver atoms similar in topology and distances to fragments of the elemental fcc-Ag. In contrast, pressure does not change significantly the O–Ag–O quasi-linear configuration, the shortest Ag–O distances and the ∠O–Ag–O angle remaining almost constant at 2.237–2.236 Å and 161.7–160.9°, respectively, between room pressure and 2.5 GPa. The other three Ag–O contacts, however, progressively decrease with pressure. As a consequence of this particular atomic arrangement in a silver-rich compound, silver is not surrounded by just 5 oxygen atoms, but also by four other Ag atoms forming [Ag(Ag$_4$O$_5$)] polyhedra (see Fig. 2b).

Upon further compression, at 3.2 GPa, new diffraction peaks appear in the X-ray diffraction pattern. Our data show that the phase transition starts at 2.9 (4) GPa. The transition is completed at 5.3 GPa. The stability of the pattern profile during several pressure points above this pressure clearly indicates the completion of the structural phase transition. Thirteen diffraction peaks of the 5.3 GPa pattern could be indexed in a monoclinic cell with lattice constants: a = 5.426 (8) Å, b = 9.405 (17) Å, c = 5.8663 (6) Å, and β = 115.97 (9) (Z = 4, V = 269.1 (5) Å^3). Therefore, the existence of a structure with such a unit-cell would imply a volume change of about 2% at the transition. The reflection conditions in the indexed lattice planes are consistent with symmetry elements of space groups $P2$, $P2_1$, Pm, Pc, $P2/m$, $P2_1/m$, $P2/c$ or $P2_1/c$. These unit-cell dimensions do not correspond to any of the polymorphs of alkaline-metal carbonates collected at the ICSD database. In Fig. 5 we show the energy-volume curves of the potential structural candidates considered: $P2_1/m$ Ag$_2$CO$_3$ [13, this work], $P3_1/c$ Ag$_2$CO$_3$-HT-I [14], P-62m Ag$_2$CO$_3$-HT-II [14], $C2/c$ K$_2$CO$_3$–I-like [37], $P2_1/c$ K$_2$CO$_3$-II-like [38], $C2/m$ Na$_2$CO$_3$-like [39] and $Pnma$ Rb$_2$CO$_3$-like [40]. Structural determination was tried using the program Endeavour [53,54], which seeks a combined global optimization of the difference between calculated and observed powder diffraction data and the potential energy of the system. Unfortunately, the structural solution process was unsuccessful for this phase. Indexed lattice parameters for this phase at different pressures are collected in Table 3. A tentative equation of state of this first high-pressure phase (HP1) could be defined by the following characteristic parameters: V$_0$ = 534 (2) Å^3, B$_0$ = 86 (5) GPa and B$'_0$ fixed to 4 (see Fig. 4). This first pressure-driven phase is stable up to 9.7 GPa.
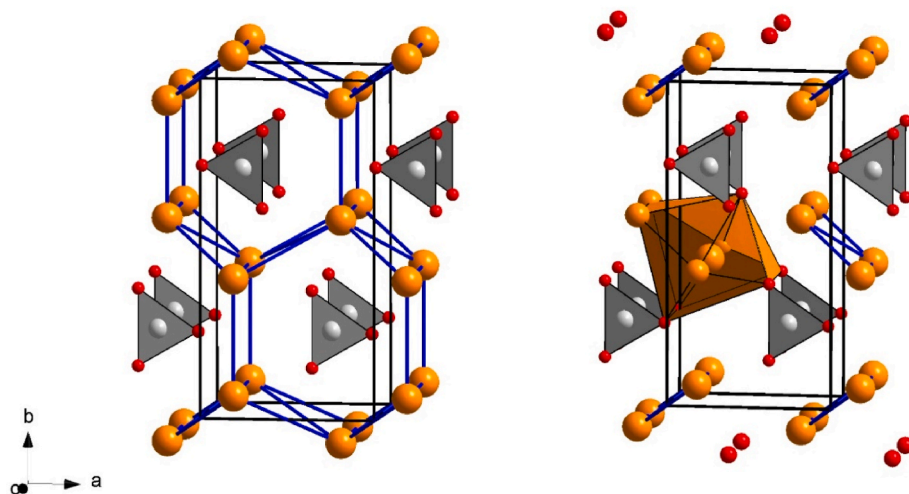
Fig. 2. Structure of the monoclinic $P2_1/m$ Ag_2CO_3 phase. Orange, grey and red spheres represent Ag, C and O atoms, respectively. The monoclinic unit cell is shown with black lines. (a) Thick blue lines show the Ag–Ag contacts below 3.61 Å at ambient conditions. (b) Silver coordination sphere consisting of 5 O atoms and 4 Ag atoms that forms a $[Ag(Ag_4O_5)]$ polyhedron. (For interpretation of the references to colour in this figure legend, the reader is referred to the Web version of this article.)
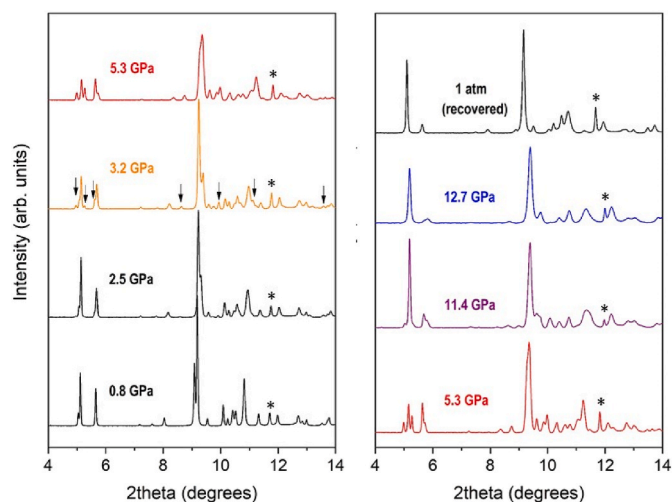

Fig. 3. Selected powder XRD patterns of Ag_2CO_3 from experiments. Backgrounds have been subtracted. (a) XRD patterns up to 5.3 GPa showing the first phase transition. (b) XRD patterns from 5.3 to 13.3 GPa and down to room pressure, showing the second phase transition and the recovery of the initial phase. The diffraction peak assigned to the (111) reflection of the Cu pressure gauge is denoted with an asterisk (*). Synchrotron radiation wavelength was 0.4246 Å.

Table 2
Experimental lattice parameters and unit-cell volumes of initial monoclinic $P2_1/m$ Ag_2CO_3 silver carbonate at different pressures and room temperature during upstroke pressure measurements.

P (GPa)	a axis (Å)	b axis (Å)	c axis (Å)	β angle (°)	Volume (Å^3)
0.05	4.851 (2)	9.547 (6)	3.254 (1)	91.97 (7)	150.6 (1)
0.15	4.850 (2)	9.546 (6)	3.249 (1)	91.82 (7)	150.3 (1)
0.2	4.849 (2)	9.545 (6)	3.245 (1)	91.78 (7)	150.2 (1)
0.25	4.848 (2)	9.542 (6)	3.242 (1)	91.71 (7)	149.9 (1)
0.32	4.846 (2)	9.539 (6)	3.237 (1)	91.63 (7)	149.6 (1)
0.42	4.843 (2)	9.534 (6)	3.233 (1)	91.48 (7)	149.2 (1)
0.5	4.841 (2)	9.533 (6)	3.226 (1)	91.38 (7)	148.8 (1)
0.6	4.839 (2)	9.530 (6)	3.217 (1)	91.28 (7)	148.3 (1)
0.8	4.832 (2)	9.519 (6)	3.207 (1)	90.95 (7)	147.5 (1)
0.82	4.835 (2)	9.521 (6)	3.210 (1)	91.00 (7)	147.8 (1)
1.0	4.828 (2)	9.516 (6)	3.196 (1)	90.67 (7)	146.8 (1)
1.0	4.831 (2)	9.518 (6)	3.200 (1)	90.77 (7)	147.2 (1)
1.1	4.826 (2)	9.518 (6)	3.191 (1)	90.56 (7)	146.6 (1)
1.25	4.824 (2)	9.510 (6)	3.185 (1)	90.39 (7)	146.1 (1)
1.4	4.821 (2)	9.505 (6)	3.178 (1)	90.23 (7)	145.6 (1)
1.65	4.821 (2)	9.504 (6)	3.174 (1)	90.17 (7)	145.3 (1)
1.9	4.815 (2)	9.493 (6)	3.159 (1)	89.90 (7)	144.4 (1)
2.2	4.810 (2)	9.481 (6)	3.150 (1)	89.69 (7)	143.6 (1)
2.5	4.806 (2)	9.476 (6)	3.141 (1)	89.49 (7)	143.0 (1)
2.7	4.799 (2)	9.472 (6)	3.130 (1)	89.23 (7)	142.3 (1)
3.2	4.791 (2)	9.470 (6)	3.119 (1)	88.95 (7)	141.5 (1)

Another transition takes place at higher pressure. Changes in the XRD patterns occur between 9.7 and 11.4 GPa (second phase transition at 10.5 (8) GPa) and the transition is completed at 12.7 GPa. The XRD pattern at this last pressure was indexed on the basis of another monoclinic cell with lattice parameters: $a = 4.681$ (5) Å, $b = 9.396$ (9) Å, $c = 2.957$ (2) Å and $\beta = 85.52$ (7)° (Z = 2, V = 129.65 (15) Å^3), comparable to those of the initial low-pressure phase. This transformation would not entail a significant volume collapse; that is, no significant volume discontinuity is found with respect to the HP1 phase. This $P2_1/m$ monoclinic structure is stable to the highest pressure reached in this study, 13.3 GPa, and during decompression down to ambient pressure. Lattice parameters of the HP2 phase at different pressures are collected in Table 4. A dense structure with atomic coordinates similar to those of the initial phase would roughly explain the XRD patterns. The recovered sample has broader diffraction peaks due to internal stresses but parameters similar to the initial one. Note that the unsolved intermediate phase was not observed in the downstroke process. This fact would be consistent with our DFT calculations that suggest that the monoclinic

phase is the thermodynamically stable structure for the Ag_2CO_3 stoichiometry in the studied pressure range. The compressibility behavior of this $P2_1/m$-Ag_2CO_3 phase has been revisited taking into account all the experimentally available data. It can be described by a zero-pressure volume $V_0 = 151.3$ (2) Å^3, bulk modulus $B_0 = 26$ (2) GPa and first-pressure derivative of the bulk modulus $B'_0 = 20$ (2). As mentioned before, the bulk modulus of this compound drastically increases upon compression.

The fact that the intermediate HP1 pressure-induced phase was not observed during decompression suggests that it could be a metastable phase produced by internal stresses due to non-hydrostatic conditions. Despite the fact that silicone oil is considered a good pressure transmitting medium below 12 GPa, a close inspection of the stresses caused by this medium in ruby chips was done by Klotz and coworkers [19]. In that study, the authors reported that an extremely sensitive criterion for solidification of the pressure transmitting medium is the standard deviation (σ) of the pressures indicated by several ruby spheres evenly distributed in the pressure chamber. This study shows that, using silicone oil, pressure differences already appear at 3 GPa and pressure gradients significantly increase with pressure up to 6 GPa, where
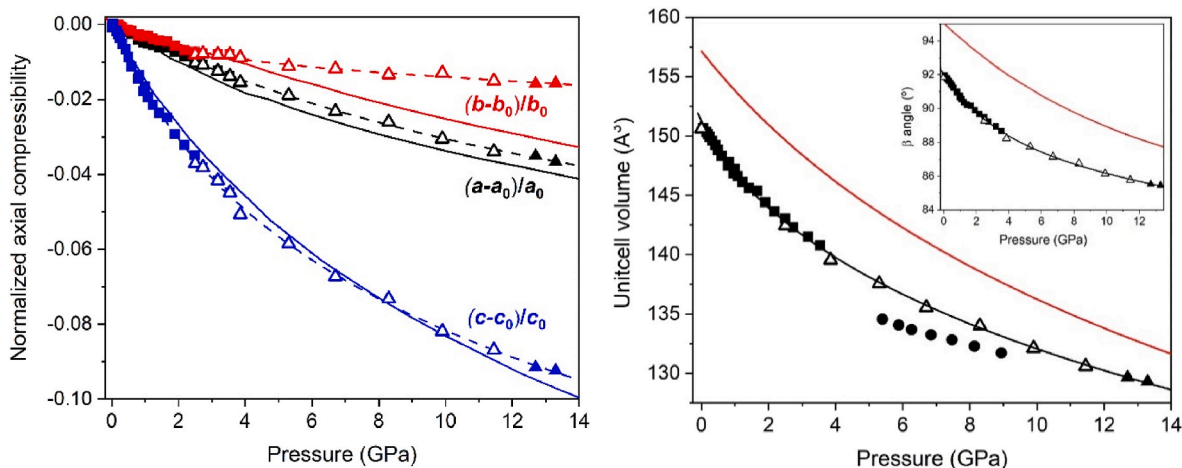
Fig. 4. (a) Relative axial compressibilities of the $P2_1/m$ Ag$_2$CO$_3$ structure. Experimental relative contractions $(a-a_0)/a_0$, $(b-b_0)/b_0$ and $(c-c_0)/c_0$ are represented as black, red and blue symbols, respectively. Solid squares and triangles denote datapoints obtained before and after the phase transition to the intermediate high-pressure metastable phase during upstroke, respectively, while empty triangles correspond to downstroke datapoints. Results from DFT calculations for $P2_1/m$ Ag$_2$CO$_3$ are depicted as solid lines. Dashed lines are fits to our experimental data. (b) Pressure-volume data per unit cell, except in the case of the intermediate phase that half of the unit-cell is depicted for the sake of comparison ($Z = 2$ in all cases). Black symbols refer to our experimental data and the black and red solid lines represent the fits of our room-temperature experimental and calculated data with a third-order Birch–Murnaghan EOS, respectively. (For interpretation of the references to colour in this figure legend, the reader is referred to the Web version of this article.)
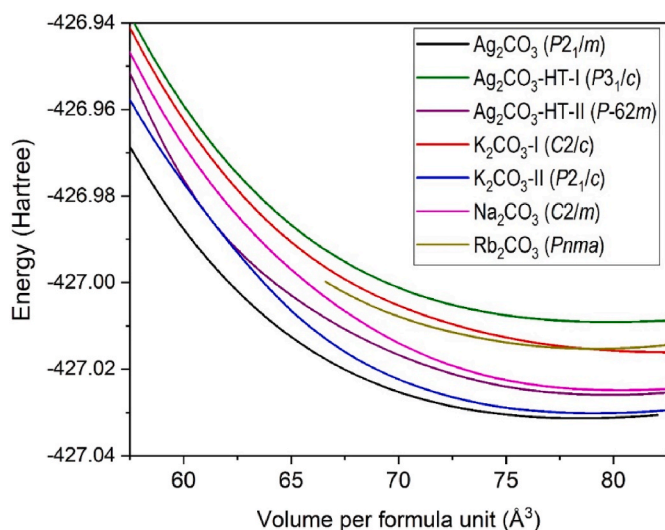

Fig. 5. Cohesive energy as a function of the volume per Ag$_2$CO$_3$ formula unit for the $P2_1/m$ Ag$_2$CO$_3$ [13, this work], $P3_1/c$ Ag$_2$CO$_3$-HT-I [14], P-62m Ag$_2$CO$_3$-HT-II [14], $C2/c$ K$_2$CO$_3$–I-like [36], $P2_1/c$ K$_2$CO$_3$-II-like [37], $C2/m$ Na$_2$CO$_3$-like [38] and $Pnma$ Rb$_2$CO$_3$-like [39] phases.

Table 3
Indexed lattice parameters and unit-cell volumes of the first Ag$_2$CO$_3$ high-pressure phase (HP1) at different pressures and room temperature.

P (GPa)	a axis (Å)	b axis (Å)	c axis (Å)	β angle (°)	Volume (Å³)
5.4	5.426 (8)	9.405 (17)	5.866 (6)	115.97 (9)	269.1 (5)
5.9	5.414 (8)	9.413 (17)	5.849 (6)	115.90 (9)	268.2 (5)
6.3	5.411 (8)	9.415 (17)	5.834 (6)	115.88 (9)	267.4 (5)
6.8	5.406 (8)	9.419 (17)	5.817 (6)	115.87 (9)	266.5 (5)
7.5	5.400 (8)	9.425 (17)	5.800 (6)	115.85 (9)	265.6 (5)
8.1	5.391 (8)	9.430 (17)	5.780 (6)	115.79 (9)	264.6 (5)
8.9	5.380 (8)	9.431 (17)	5.762 (6)	115.71 (9)	263.4 (5)

gradients were typically 0.4 GPa. Surprisingly, these gradients decrease as the average pressure increases and reach a very low value of 1–2 kbar at 12 GPa (see Fig. 6). This anomalous behavior is a direct consequence

Table 4
Experimental lattice parameters and unit-cell volumes of HP2 monoclinic $P2_1/m$ Ag$_2$CO$_3$ silver carbonate at different pressures and room temperature. "up" and "down" denote upstroke and downstroke pressure measurements.

P (GPa)	a axis (Å)	b axis (Å)	c axis (Å)	β angle (°)	Volume (Å³)
12.7 (up)	4.681 (5)	9.396 (9)	2.957 (2)	85.53 (7)	129.65 (15)
13.3 (up)	4.674 (5)	9.397 (9)	2.954 (2)	85.45 (7)	129.30 (15)
11.5 (down)	4.687 (5)	9.403 (9)	2.972 (2)	85.76 (7)	130.60 (15)
9.9 (down)	4.703 (5)	9.423 (9)	2.988 (2)	86.14 (7)	132.12 (16)
8.3 (down)	4.725 (5)	9.419 (9)	3.016 (2)	86.74 (7)	134.02 (16)
6.7 (down)	4.739 (5)	9.434 (9)	3.036 (2)	87.14 (7)	135.54 (16)
5.3 (down)	4.760 (5)	9.441 (9)	3.064 (2)	87.74 (7)	137.57 (17)
3.85 (down)	4.776 (2)	9.462 (9)	3.089 (2)	88.23 (7)	139.56 (14)
2.5 (down)	4.801 (2)	9.470 (9)	3.134 (2)	89.29 (7)	142.47 (14)
0.0001 (down)	4.851 (2)	9.553 (8)	3.2514 (13)	91.86 (4)	150.61 (12)

of a phase transition in silicone oil as detected by IR absorption. This would explain why, experimentally, the initial Ag$_2$CO$_3$ $P2_1/m$ structure transforms into a metastable phase at 3 GPa and reappears at 10.5 GPa, once better hydrostatic conditions are recovered. The absence of any phase transition in Ag$_2$CO$_3$ during the decompression could be related to the possible hysteresis of the phase transition of the silicone oil.

The volumetric thermal expansion (α) of this carbonate at pressures between 2 and 3 GPa has been estimated. Due to the fact that the pressure was not constant during heating, we calculated the relative increase in volume $(V_{P,T} - V_{ref})/V_{P,T}$ at each P-T datapoint using a reference volume at each pressure (V_{ref}) obtained from the room-temperature (T_{ref}) bulk modulus [22]. A linear fitting according to the expression $(V_{P,T} - V_{ref})/V_{P,T} = \alpha(T - T_{ref})$ in the 20–240 °C temperature range yields a volumetric thermal expansion of $7.8\,(4) \cdot 10^{-5}$ K^{-1}. This value is slightly smaller than that reported by Norby et al. who give $9.1 \cdot 10^{-5}$ K^{-1} at ambient pressure [14]. No signs of any structural phase

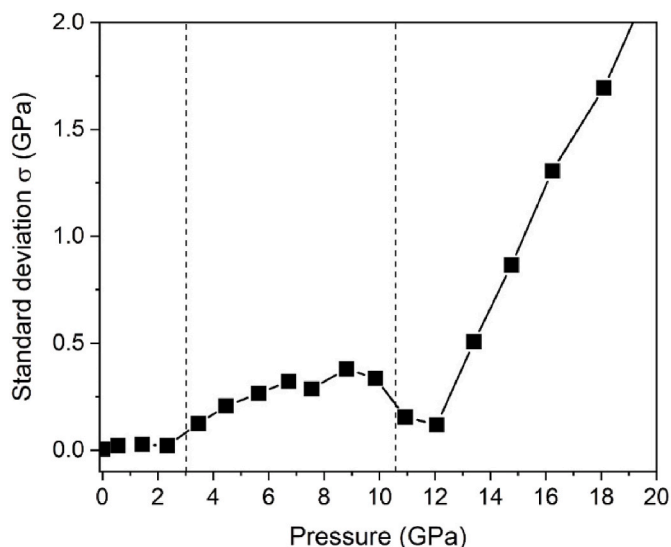**Fig. 6.** Digitalized data of the pressure dependence of the standard deviation σ for silicone oil as reported in Fig. 4 of Reference [19]. Vertical dashed lines mark the location of the observed phase transitions in Ag_2CO_3.

transition was observed up to 3.1 and 512 K.

5. Conclusions

We have reported X-ray diffraction measurements at high-pressure (and high-temperature) in Ag2CO3 up to 13.3 GPa along with DFT calculations. Silver carbonate has a characteristic structure at ambient conditions, with short Ag–Ag metallic distances, some of them similar to those existing in metallic fcc-Ag. Moreover, the arrangement of the Ag atoms also partially resembles that of elemental silver, with the existence of corrugated hexagonal layers. The anisotropic compression of the initial monoclinic $P2_1/m$ structure shows that the c axis is by far the most compressible mainly due to the decrease of the Ag–Ag distances.

At pressures beyond 2.9 (4) GPa, the appearance of new diffraction peaks in the XRD patterns reveals a structural phase transition. This high-pressure phase, whose unit-cell was tentatively identified, was stable to 10.5 (9) GPa. Above that pressure, the initial $P2_1/m$ structure is recovered, it is maintained to the maximum pressure reached in this study, 13.3 GPa, and down to ambient conditions during the whole decompression process. This anomalous behavior was explained in terms of the viscoelastic properties of the silicone oil used as pressure transmitting medium in our experiments. It was reported that this polydimethyl-siloxane oil has an interval of non-hydrostatic stresses between 3 and 10 GPa, which coincides with the pressure range in which the metastable intermediate pressure-induced phase is observed.

We have determined the compressibility, the anisotropy and the thermal expansion of silver carbonate. Our data shows that this compound presents a bulk modulus that rapidly increases with pressure (B′0 = 10 (3) or 20 (2) depending on the 0–2.5 or 0–13.3 GPa datasets considered). Such a strong increase in bulk modulus is intimately related to the compressibility behavior of the Ag–Ag distances. The crystal chemistry of silver carbonate seems therefore to be determined by the closed-shell d10-d10 interactions between Ag atoms, which entail the existence of silver subarrays and irregular coordination environments and their preservation upon compression.

Author contributions

Conceptualization, D.S.P, Investigation, D.S.P., L.P., R. Ch.J., A.O.R., J.R.F. and C.P, Formal analysis, R.Ch.J., L.P., D.S.P., and A.O.R, Writing – original draft, R.Ch.J., D.S.P, Writing - review & editing, all the

authors.

Declaration of competing interest

The authors declare that they have no known competing financial interests or personal relationships that could have appeared to influence the work reported in this paper.

Data availability

Data will be made available on request.

References

[1] UNESCO Strategy for Action on Climate Change, 39th UNESCO General Conference, 2017, 39 C/46.

[2] H.E. Dunsmore, A geological perspective on global warming and the possibility if carbon dioxide removal as calcium carbonate mineral, Energy Convers. Mgmgt. 33 (1992) 565, https://doi.org/10.1016/0196-8904(92)90057-4.

[3] K.S. Lackner, C.H. Wendt, D.P. Butt, E.L. Joyce, D.H. Sharp, Carbon dioxide: disposal in carbonate minerals, Energy 20 (1995) 1153, https://doi.org/10.1016/0360-5442(95)00071-N.

[4] K.S. Lackner, Carbonate chemistry for sequestering fossil carbon, Annu. Rev. Energy Environ. 27 (2002) 193, https://doi.org/10.1146/annurev.energy.27.122001.083433.

[5] S.O. Snæbjörnsdóttir, B. Sigfusson, Ch Marieni, D. Golberg, S.R. Gislason, E. H. Oelkers, Carbon dioxide storage through mineral carbonation, Nat. Rev. Earth Environ. 1 (2020) 90–102, https://doi.org/10.1038/s43017-019-0011-8.

[6] D. Santamaria-Perez, C. McGuire, A. Makhluf, A. Kavner, R. Chulia-Jordan, J. L. Jorda, F. Rey, J. Pellicer-Porres, D. Martinez-Garcia, P. Rodriguez-Hernandez, A. Muñoz, Correspondence: strongly-driven Re + CO2 redox reaction at high-pressure and high-temperature, Nat. Commun. 7 (2016), 13647, https://doi.org/10.1038/ncomms13647.

[7] D. Santamaria-Perez, C. McGuire, A. Makhluf, A. Kavner, R. Chulia-Jordan, J. Pellicer-Porres, D. Martinez-Garcia, A. Doran, M. Kunz, P. Rodriguez-Hernandez, A. Muñoz, Exploring the chemical reactivity between carbon dioxide and three transition metals (Au, Pt, Re) at high-pressure, high-temperature conditions, Inorg. Chem. 55 (2016) 10793–10799, https://doi.org/10.1021/acs.inorgchem.6b01858.

[8] D. Santamaria-Perez, J. Ruiz-Fuertes, M. Peña-Alvarez, R. Chulia-Jordan, T. Marqueño, D. Zimmer, V. Gutierrez-Cano, S. MacLeod, E. Gregoryanz, C. Popescu, P. Rodriguez-Hernandez, A. Muñoz, Post-tilleyite, a dense calcium silicate-carbonate phase, Sci. Rep. 9 (2019) 7898, https://doi.org/10.1038/s41598-019-44326-9.

[9] H. Herzog, Carbon sequestration via mineral carbonation: overview and assessment. Report of the carbon sequestration initiative. https://sequestration.mit.edu/pdf/carbonates.pdf, 2002.

[10] A. Sanna, M. Uibu, G. Caramanna, R. Kuusik, M.M. Maroto-Valer, A review of mineral carbonation technologies to sequester CO_2, Chem. Soc. Rev. 43 (2014) 8049–8080, https://doi.org/10.1039/C4CS00035H.

[11] W.J. Culbertson Jr., Investigation and Design of a Regenerable Silver Oxide System for Carbon Dioxide Control, 1964. Report AD0612021 Defense Technical Information Center, https://apps.dtic.mil/sti/pdfs/AD0612021.pdf.

[12] J.M. Hart, J.B. Borghese, C.H. Chang, R.J. Cusick, Portable life support system regenerative carbon dioxide and water vapor removal by metal oxide absorbents preprototype hardware development and testing, SAE Transactions, J. Aerospace 101 (1992) 987–996. http://www.jstor.org/stable/44733052.

[13] R. Masse, J.C. Guitel, A. Durif, Structure du Carbonate d'Argent, Acta Crystallogr. B35 (1979) 1428–1429, https://doi.org/10.1107/S0567740879006592.

[14] P. Norby, R. Dinnebier, A.N. Fitch, Decomposition of silver carbonate; the crystal structure of two high-temperature modifications of Ag_2CO_3, Inorg. Chem. 41 (2002) 3628–3637, https://doi.org/10.1021/ic0111177.

[15] Y. Sawada, K. Manabe, Thermal decomposition of silver carbonate, J. Therm. Anal. 37 (1991) 1657–1663, https://doi.org/10.1007/BF01912194.

[16] Y. Sawada, N. Kanou, N. Mizutani, Thermal decomposition of silver carbonate. High pressure differential thermal analysis under an atmosphere of carbon dioxide, Thermochim. Acta 183 (1991) 279–287, https://doi.org/10.1016/0040-6031(91)80464-T.

[17] F. Fauth, I. Peral, C. Popescu, M. Knapp, The new material science powder diffraction beamline at ALBA synchrotron, Powder Diffr. 28 (2013) S360, https://doi.org/10.1017/S0885715613000900.

[18] Y. Shen, R.S. Kumar, M. Pravia, M.F. Nicol, Characteristics of silicone fluid as a pressure transmitting medium in diamond anvil cells, Rev. Sci. Instrum. 75 (2004) 4450, https://doi.org/10.1063/1.1786355.

[19] S. Klotz, J.C. Chervin, P. Munsch, G. Le Marchand, Hydrostatic limits of 11 pressure transmitting media, J. Phys. D Appl. Phys. 42 (2009), 075413, https://doi.org/10.1088/0022-3727/42/7/075413.

[20] A. Dewaele, P. Loubeyre, M. Mezouar, Equations of state of six metals above 94 GPa, Phys. Rev. B 70 (2004), 094112, https://doi.org/10.1103/PhysRevB.70.094112.

[21] D. Santamaria-Perez, A. Otero-de-la-Roza, J. Ruiz-Fuertes, R. Chulia-Jordan, T. Marqueño, S. MacLeod, C. Popescu, Pressure and temperature effects on low-density $Mg_3Ca(CO_3)_4$ huntite carbonate, J. Phys. Chem. C 124 (2020) 1077–1087, https://doi.org/10.1021/acs.jpcc.9b08952.

[22] D. Santamaria-Perez, J. Ruiz-Fuertes, T. Marqueño, J. Pellicer-Porres, R. Chulia-Jordan, S. MacLeod, C. Popescu, Structural behavior of natural silicate−carbonate spurrite mineral, $Ca_5(SiO_4)_2(CO_3)$, under high-pressure, high-temperature conditions, Inorg. Chem. 57 (2018) 98–105, https://doi.org/10.1021/acs.inorgchem.7b02101.

[23] R. Chuliá-Jordán, D. Santamaría-Perez, A. Otero-de-la-Roza, J. Ruiz-Fuertes, T. Marqueño, O. Gomis, S. MacLeod, C. Popescu, Phase stability of natural $Ni_{0.75}Mg_{0.22}Ca_{0.03}CO_3$ gaspeite mineral at high pressure and temperature, J. Phys. Chem. C 124 (2020) 19781–19792, https://doi.org/10.1021/acs.jpcc.0c04509.

[24] Y. Wang, J. Zhang, H. Xu, Z. Lin, L.L. Daemen, Y. Zhao, L. Wang, Thermal equation of state of copper studied by high P-T synchrotron x-ray diffraction, Appl. Phys. Lett. 94 (2009), 071904, https://doi.org/10.1063/1.3085997.

[25] C. Prescher, V.B. Prakapenka, DIOPTAS: a program for reduction of two-dimensional X-ray diffraction data and data exploration, High Pres. Res. 35 (2015) 223–230, https://doi.org/10.1080/08957959.2015.1059835.

[26] T.J.B. Holland, S.A.T. Redfern, Unit cell refinement from powder diffraction data: the use of regression diagnostics, Mineral. Mag. 61 (1997) 65–77, https://doi.org/10.1180/minmag.1997.061.404.07.

[27] G. Nolze, W. Kraus, Powdercell 2.0 for windows, Powder Diffr. 13 (1998) 256–259.

[28] J. Rodriguez-Carvajal, Recent advances in magnetic structure determination by neutron powder diffraction, Phys. B 192 (1993) 55–69, https://doi.org/10.1016/0921-4526(93)90108-I.

[29] P.E. Blöch, Projector augmented-wave method, Phys. Rev. B 50 (1994), 17953, https://doi.org/10.1103/PhysRevB.50.17953.

[30] P. Giannozzi, et al., Advanced capabilities for materials modelling with Quantum ESPRESSO, J. Phys. Condens. Matter 29 (2017), 465901, https://doi.org/10.1088/1361-648X/aa8f79.

[31] A.D. Becke, On the large-gradient behavior of the density functional exchange energy, J. Chem. Phys. 85 (1986) 7184, https://doi.org/10.1063/1.451353.

[32] J.P. Perdew, K. Burke, M. Ernzerhof, Generalized gradient approximation made simple, Phys. Rev. Lett. 77 (1996) 3865–3868, https://doi.org/10.1103/PhysRevLett.77.3865.

[33] E.R. Johnson, The exchange-hole dipole moment dispersion model, in: Non-covalent Interactions in Quantum Chemistry and Physics, Elsevier, 2017, pp. 169–194 (chapter 5), pgs.

[34] A.D. Becke, E.R. Johnson, Exchange-hole dipole moment and the dispersion interaction revisited, J. Chem. Phys. 127 (2007), 154108, https://doi.org/10.1063/1.2795701.

[35] A. Otero-de-la-Roza, E.R. Johnson, Van der Waals interactions in solids using the exchange-hole dipole moment model, J. Chem. Phys. 136 (2012), 174109, https://doi.org/10.1063/1.4705760.

[36] A. Dal Corso, Pseudopotentials periodic table: from H to Pu, Comput. Mater. Sci. 95 (2014) 337–350, https://doi.org/10.1016/j.commatsci.2014.07.043.

[37] H.Y. Becht, R. Struikmans, A monoclinic high-temperature modification of potassium carbonate, Acta Crystallogr. B 32 (1976) 3344–3346, https://doi.org/10.1107/S0567740876010303.

[38] B.M. Gatehouse, D.J. Lloyd, Crystal structure of anhydrous potassium carbonate, Dalton Trans. 70 (1973) 72, https://doi.org/10.1039/DT9730000070.

[39] A. Arakcheeva, L. Bindi, P. Pattison, N. Meisser, G. Chapuis, I. Pekov, The incommensurately modulated structures of natural natrite at 120 and 293 K from syncrotron X-ray data, Am. Mineral. 9 (2010) 574–581, https://doi.org/10.2138/am.2010.3384.

[40] R.E. Dinnebier, S. Vensky, M. Jansen, J.C. Hanson, Crystal structures and topochemical aspects of the high-temperature phases and decomposition products of the alkali-metal oxalates $M2[C2O4]$ (M=K, Rb, Cs), Chem. Eur J. 11 (2005) 1119–1129, https://doi.org/10.1002/chem.200400616.

[41] A. Otero-de-la-Roza, V. Luaña, Gibbs2: a new version of the quasi-harmonic model code. I. Robust treatment of the static data, Comput. Phys. Commun. 182 (2011) 1708–1720, https://doi.org/10.1016/j.cpc.2011.04.016.

[42] A. Otero-de-la-Roza, D. Abbasi-Perez, V. Luaña, Gibbs2: a new version of the quasi-harmonic model code. II. Models for solid-state thermodynamics, features and implementation, Comput. Phys. Commun. 182 (2011) 2232–2248, https://doi.org/10.1016/j.cpc.2011.05.009.

[43] A. Vegas, M. Jansen, Structural relationships between cations and alloys; an equivalence between oxidation and pressure, Acta Crystallogr. B 58 (2002) 38–51, https://doi.org/10.1107/S0108768101019310.

[44] D. Santamaria-Perez, A. Vegas, The Zintl-Klemm concept applied to cations in oxides. I. The structures of ternary aluminates, Acta Crystallogr. B 59 (2003) 305–323, https://doi.org/10.1107/S0108768103005615.

[45] D. Santamaria-Perez, A. Vegas, F. Liebau, The Zintl-Klemm concept applied to cations in oxides. II. The structures of silicates, Struct. Bond 118 (2005) 121–177, https://doi.org/10.1007/b137470.

[46] R. Chuliá-Jordan, D. Santamaria-Perez, J. Pellicer-Porres, A. Otero-de-la-Roza, D. Martinez-Garcia, B. Garcia-Domene, O. Gomis, J.A. Sans, K.A. Vanaja, A.S. Asha, C. Popescu, Transition path to a dense efficient-packed post-delafossite phase. Crystal structure and evolution of the chemical bonding, J. Alloys Compd. 867 (2021), 159012, https://doi.org/10.1016/j.jallcom.2021.159012.

[47] F. Birch, Finite strain isotherm and velocities for single-crystal and polycrystalline NaCl at high pressures and 300 K, J. Geophys. Res. 83 (1978) 1257.

[48] J. Zhang, R.J. Reeder, Comparative compressibilities of calcite-structure carbonates, Am. Mineral. 84 (1999) 861–870.

[49] N.L. Ross, R.J. Reeder, High-pressure structural study of dolomite and ankerite, Am. Mineral. 77 (1992) 412–421.

[50] R. Chulia-Jordan, D. Santamaria-Perez, J. Ruiz-Fuertes, A. Otero-de-la-Roza, C. Popescu, Crystal structure of $BaCa(CO_3)_2$ alstonite carbonate and its phase stability upon compression, ACS Earth Planet Chem 5 (2021) 1130–1139, https://doi.org/10.1021/acsearthspacechem.1c00032.

[51] R. Chulia-Jordan, D. Santamaria-Perez, J. Ruiz-Fuertes, A. Otero-de-la-Roza, C. Popescu, Compressibility and phase stability of iron-rich ankerite, Minerals 11 (2021) 607, https://doi.org/10.3390/min11060607.

[52] R. Chulia-Jordan, D. Santamaria-Perez, J. Gonzalez-Platas, J. Ruiz-Fuertes, A. Otero-de-la-Roza, C. Popescu, Phase stability and dense polymorph of the BaCa (CO3)2 barytocalcite carbonate, Sci. Rep. 12 (2021) 7413, https://doi.org/10.1038/s41598-022-11301-w.

[53] Crystal-Impact-GbR, 2004. Bonn, Germany, http://crystalimpact.com/endeavour.

[54] D. Santamaria-Perez, J. Haines, U. Amador, E. Moran, A. Vegas, Structural characterization of a new high-pressure phase of GaAsO4, Acta Crystallogr. B 62 (2006) 1019–1024, https://doi.org/10.1107/S0108768106039760.